Boiling peak heat flux for steady inhomogeneous heat transfer in superfluid ^{4}He

Sosuke Inui [1,2] Mikai Hulse [1,3] Toshiaki Kanai [1,3] and Wei Guo [1,2,*]

[1]*National High Magnetic Field Laboratory, 1800 East Paul Dirac Drive, Tallahassee, Florida 32310, USA*

[2]*Mechanical Engineering Department, FAMU-FSU College of Engineering, Florida State University, Tallahassee, Florida 32310, USA*

[3]*Department of Physics, Florida State University, Tallahassee, Florida 32310, USA*

(Received 9 October 2023; revised 5 November 2023; accepted 6 November 2023; published 16 November 2023)

Superfluid helium-4 (He II) is a widely adopted coolant in scientific and engineering applications owing to its exceptional heat transfer capabilities. However, boiling can spontaneously occur on a heating surface in He II when the heat flux exceeds a threshold value q^*, referred to as the peak heat flux. While the parameter q^* holds paramount importance in the design of He II based cooling systems, extensive research has primarily focused on its behavior in steady homogeneous heat transfer from a flat heating surface. For inhomogeneous heat transfer from curved surfaces, q^* exhibits intricate dependence on parameters such as the He II bath temperature T_b, the immersion depth h, and the curvature radius R_0 of the heating surface. A comprehensive understanding on how q^* depends on these parameters remains elusive. In this paper, we report our systematic study on q^* for steady heat transfer from cylindrical and spherical heaters in He II. We compute q^* for a wide range of parameter combinations (T_b, h, R_0) by solving the He II two-fluid equations of motion. The generated data have allowed us to develop a robust correlation that accurately reproduces q^* for all the parameter combinations we explored. Our findings, particularly the establishment of the correlation, carry valuable implications for emergent applications that involve steady inhomogeneous heat transfer in He II systems.

DOI: 10.1103/PhysRevB.108.174509

I. INTRODUCTION

Saturated liquid ^{4}He becomes a superfluid at temperatures below about 2.17 K [1]. In the superfluid phase (known as He II), the liquid can be considered phenomenologically as a mixture of two miscible fluid components: an inviscid superfluid that carries no entropy and a viscous normal fluid that consists of thermal quasiparticles (i.e., phonons and rotons) [2]. Heat transfer in this two-fluid system is via a unique internal convection process known as thermal counterflow. In a counterflow, the normal fluid carries the heat and moves away from a heating surface at a velocity $v_n = q/\rho s T$, where q is the heat flux, T is the He II temperature, and ρ and s are the He II density and specific entropy, respectively; the superfluid moves in the opposite direction at a velocity $v_s = -v_n \rho_n/\rho_s$ so that the net mass flow remains zero (here ρ_n and ρ_s are the densities of the normal fluid and the superfluid, respectively). This counterflow mode is extremely effective, which renders He II a valuable coolant in a wide array of scientific and engineering applications, such as for cooling superconducting particle accelerator cavities, superconducting magnets, medical instruments, and even satellites [3].

When the relative velocity of the two fluids in counterflow exceeds a small critical value [4], a chaotic tangle of quantized vortex lines can develop spontaneously in the superfluid. These quantized vortices are filamentary topological defects, each carrying a quantized circulation $\kappa \simeq 10^{-3}$ cm^2/s around its angstrom-sized core [5]. A mutual friction force between the two fluids then emerges due to thermal quasiparticles scattering off the quantized vortices [6]. This mutual friction can lead to novel flow characteristics in both fluids [7–11]. When the heat flux is further increased to above a threshold value q^*, referred to as the peak heat flux, boiling on the heating surface can occur. This boiling action leads to the formation of vapor bubbles and these bubbles can act as effective insulators between the heating surface and the surrounding He II, which impairs the heat transfer and results in the potential for overheating and damage to the cooled devices.

Developing a reliable correlation for assessing q^* is of great importance in the design of He II based cooling systems. The value of q^* can depend on many parameters, such as the heating duration Δt, the temperature of the He II bath T_b, the immersion depth h, and the curvature radius R_0 of the heating surface. In this paper, we shall focus on q^* in steady heat transfer where $\Delta t \to \infty$, since this knowledge lays the groundwork for future explorations of q^* within transient heat transfer scenarios.

There have been extensive studies on q^* in the context of steady, homogeneous heat transfer of He II within uniform channels driven by planar heaters [12–16]. The relationship between q^* and the parameters T_b and h has been reasonably well understood [3]. However, when it comes to inhomogeneous heat transfer from curved surfaces such as cylindrical and spherical surfaces, q^* displays intricate dependencies on the parameter combination (T_b, h, R_0). Despite some past studies on q^* for these nonuniform geometries [17–22], a systematic understanding on how q^* varies with the parameter combination (T_b, h, R_0) remains absent. Nevertheless, establishing the capability to reliably predict q^* values in

*Corresponding author: wguo@magnet.fsu.edu

these nonuniform geometries holds significant importance for specific applications, such as cooling superconducting transmission lines and magnet coils [23,24], detecting pointlike quench spots on superconducting accelerator cavities [25,26], and emerging applications like the development of hot-wire anemometry for studying quantum turbulence in He II [27].

In this paper, we present a comprehensive numerical investigation of q^* in steady, nonhomogeneous heat transfer from both cylindrical and spherical heating surfaces submerged in He II. We employ the He II two-fluid equations of motion to compute q^* over a wide range of parameter combinations (T_b, h, R_0). Furthermore, we demonstrate that the data we generate can facilitate the development of a robust correlation capable of accurately reproducing q^* across all the parameter combinations we explore. The paper is structured as follows: we begin by outlining our theoretical model in Sec. II. In Sec. III, we conduct a comparative analysis of the calculated q^* values for heat transfer from cylindrical heaters against available experimental data to calibrate our model. In Sec. IV A, we present a systematic computation of q^* using the fine-tuned model for cylindrical heaters under varying parameter combinations (T_b, h, R_0) and establish a reliable correlation linking q^* with these parameters. In Sec. IV B, we provide a similar analysis and correlation for q^* concerning heat transfer from spherical heaters. We conclude with a summary in Sec. V.

II. THEORETICAL MODEL

We employ the two-fluid hydrodynamic model in our current research, which was also utilized in our prior work to analyze transient heat transfer in He II [28,29]. A comprehensive description of this model is available in Refs. [30,31]. In brief, this model is based on the conservation laws governing He II mass, momentum, and entropy. It comprises four evolution equations for He II's total density ρ, total momentum density $\rho\boldsymbol{v} = \rho_s\boldsymbol{v}_s + \rho_n\boldsymbol{v}_n$, superfluid velocity $\boldsymbol{v}_s$, and entropy s, as follows:

$$\frac{\partial\rho}{\partial t} + \nabla\cdot(\rho\boldsymbol{v}) = 0, \tag{1}$$

$$\frac{\partial(\rho\boldsymbol{v})}{\partial t} + \nabla\left(\rho_s v_s^2 + \rho_n v_n^2\right) + \nabla P = 0, \tag{2}$$

$$\frac{\partial\boldsymbol{v}_s}{\partial t} + \boldsymbol{v}_s\cdot\nabla\boldsymbol{v}_s + \nabla\mu = \frac{\boldsymbol{F}_{ns}}{\rho_s}, \tag{3}$$

$$\frac{\partial(\rho s)}{\partial t} + \nabla\cdot(\rho s\boldsymbol{v}_n) = \frac{\boldsymbol{F}_{ns}\cdot\boldsymbol{v}_{ns}}{T}, \tag{4}$$

where P is the pressure, μ is the chemical potential of He II, $\boldsymbol{v}_{ns} = \boldsymbol{v}_n - \boldsymbol{v}_s$ is the relative velocity between two fluids, and $\boldsymbol{F}_{ns}$ is the Gorter–Mellink mutual friction between the two fluids per unit volume of He II [3].

$\boldsymbol{F}_{ns}$ can be expressed in terms of $\boldsymbol{v}_{ns}$ and the vortex-line density L as [32,33]

$$\boldsymbol{F}_{ns} = \frac{\kappa}{3}\frac{\rho_s\rho_n}{\rho}B_L L\boldsymbol{v}_{ns}, \tag{5}$$

where B_L is a temperature dependent mutual friction coefficient [34]. The calculation of $\boldsymbol{F}_{ns}$ requires the evolution of $L(\boldsymbol{r}, t)$, for which we employ Vinen's equation [6]

$$\frac{\partial L}{\partial t} + \nabla\cdot(\boldsymbol{v}_{\mathrm{L}}L) = \alpha_{\mathrm{V}}|\boldsymbol{v}_{ns}|L^{\frac{3}{2}} - \beta_{\mathrm{V}}L^2 + \gamma_{\mathrm{V}}|\boldsymbol{v}_{ns}|^{\frac{5}{2}}, \tag{6}$$

where α_V, β_V, and γ_V are temperature-dependent empirical coefficients [6] and $\boldsymbol{v}_{\mathrm{L}}$ represents the vortex-tangle drift velocity, which is often approximated as equal to the local superfluid velocity $\boldsymbol{v}_s$ [35,36].

Similar to the previous works [28,29], we include correction terms that depend on v_{ns}^2 for He II's thermodynamic properties, as suggested by Landau [2,37], to account for the large v_{ns} values under high heat flux conditions in the current research:

$$\mu(P, T, v_{ns}) = \mu^{(s)}(P, T) - \frac{1}{2}\frac{\rho_n}{\rho}v_{ns}^2, \tag{7}$$

$$s(P, T, v_{ns}) = s^{(s)}(P, T) + \frac{1}{2}v_{ns}^2\frac{\partial(\rho_n/\rho)}{\partial T}, \tag{8}$$

$$\rho(P, T, v_{ns}) = \rho^{(s)}(P, T) + \frac{1}{2}\rho^2 v_{ns}^2\frac{\partial(\rho_n/\rho)}{\partial P}, \tag{9}$$

where the quantities with the superscript "(s)" represent static values, which can be obtained from the HEPAK dynamic library [38]. The two-fluid model outlined above provides a coarse-grained description of the He II hydrodynamics, since it does not resolve the interaction between individual vortices and the normal fluid [39–41]. Nonetheless, prior research has shown that this model describes nonisothermal flows in the He II well when L is reasonably high [28,42].

Since our current research focuses on the steady-state heat transfer, we drop the terms that involve the time derivative in the governing equations and reformulate them in a manner convenient for numerical solutions. For instance, Eq. (1) leads to

$$\rho_s\boldsymbol{v}_s = -\rho_n\boldsymbol{v}_n. \tag{10}$$

Moreover, by integrating Eq. (2), we can derive an expression for $P(r)$ as

$$P(r) = P_b - \rho_s v_s^2 - \rho_n v_n^2. \tag{11}$$

Here the bath pressure $P_b = P_S(T_b) + \rho gh$, where $P_S(T_b)$ represents the saturation pressure at the bath temperature T_b, g stands for gravitational acceleration, and h denotes the immersion depth of the heating surface. The last two terms in Eq. (11) account for the Bernoulli pressures associated with the flows in the two fluids. Now, assuming axial symmetry and recognizing the identity $d\mu = \frac{1}{\rho}dP - sdT$ [2], we can express Eq. (3) in the following form, utilizing Eqs. (2) and (10):

$$\rho v_s\frac{\partial v_n}{\partial r} + \partial_r(\rho v_n v_s) = \rho s\frac{\partial T}{\partial r} + \frac{\rho}{\rho_s}F_{ns}. \tag{12}$$

The temperature $T(r)$ at location r can be obtained by integrating the above equation as

$$T(r) = T_b + \int_r^\infty dr' G(r'), \tag{13}$$

where

$$G(r) := \frac{1}{\rho_s s}F_{ns} - \frac{v_s}{s}\partial_r v_n - \frac{1}{\rho s}\partial_r(\rho v_n v_s). \tag{14}$$

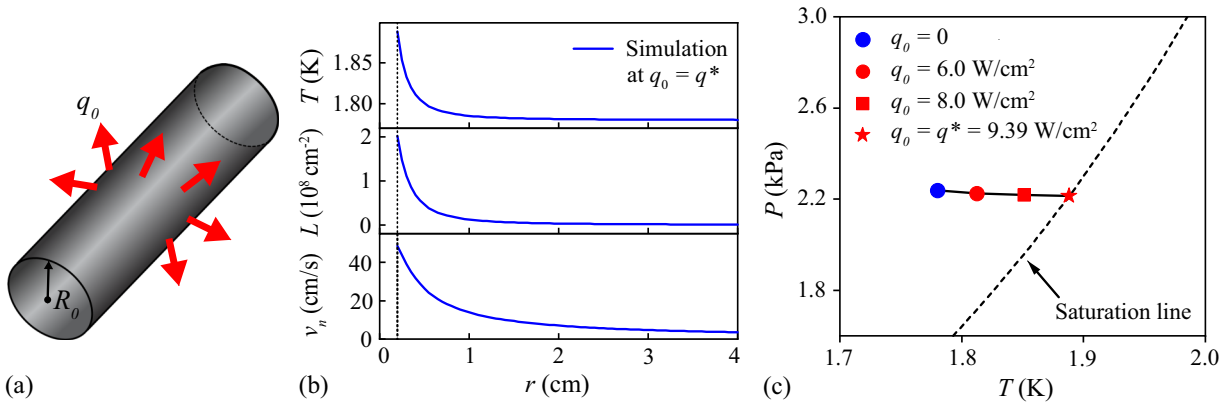

FIG. 1. (a) Schematic diagram of a long cylindrical heater of radius R_0 with a constant surface heat flux q_0. (b) Simulated profiles of temperature $T(r)$ (top), vortex-line density $L(r)$ (middle), and normal-fluid velocity $v_n(r)$ (bottom) at q_0 close to 9.39 W/cm^2 with $T_b = 1.78$ K, $R_0 = 0.2$ cm, and $h = 50$ cm. (c) The calculated state parameter (P_0, T_0) of the He II on the heater surface at various applied q_0, indicated by the solid circles, squares, and stars.

Next, we integrate Eq. (4) from the heater surface R_0 to r to obtain $v_n(r)$ as

$$v_n(r) = \frac{R_0^N \rho_0 s_0}{r^N \rho s} v_{n0} + \frac{1}{r^N \rho s} I(r), \tag{15}$$

where

$$I(r) := \int_{R_0}^{r} dr' r'^N \frac{F_{ns}(r') v_{ns}(r')}{T(r')}. \tag{16}$$

The quantities with the subscript "0" in the above equations indicate their values at $r = R_0$ and the parameter N assumes values of 1 or 2, corresponding to cylindrical and spherical coordinates, respectively. Note that v_{n0} is related to the surface heat flux q_0 as $v_{n0} = q_0/\rho_0 s_0 T_0$, which transforms Eq. (15) into

$$v_n(r) = \frac{q_0}{\rho s T_0} \left(\frac{R_0}{r}\right)^N + \frac{I(r)}{r^N \rho s}. \tag{17}$$

Finally, within the parameter ranges explored in our current research, it becomes evident that the drift term $\nabla \cdot (\boldsymbol{v}_L L)$ and the term $\gamma_V |\boldsymbol{v}_{ns}|^{\frac{5}{2}}$ in Eq. (6) are orders of magnitude smaller than the remaining terms. By omitting these two terms, we can deduce that $L(r) = \gamma^2 v_{ns}(r)^2$, where γ is related to the empirical coefficients α_V and β_V introduced in Eq. (6) as $\gamma = \alpha_V/\beta_V$. Therefore, F_{ns} can be calculated as

$$F_{ns} = \frac{\kappa}{3} \frac{\rho_s \rho_n}{\rho} B_L \gamma^2 v_{ns}^3. \tag{18}$$

We must emphasize that Eq. (6) was originally proposed for homogeneous and isotropic counterflow. There are ongoing discussions regarding potential modifications of this equation for nonuniform flows [43–45]. In our present research, we will maintain the use of Eq. (18). However, we will adapt the γ values, originally derived for uniform counterflow [46–48], to best fit the available data under nonuniform counterflow conditions. The relevant details are provided in Sec. III.

Equations (10), (11), (13), (17), and (18) now form the base of our iterative numerical approach for solving the steady-state heat transfer problems involving cylindrical and spherical heaters. The iteration starts with constant He II properties $P^{(0)} = P_b$, $T^{(0)} = T_b$, and a prescribed normal-fluid velocity profile $v_n^{(0)}(r) = \frac{q_0}{\rho^{(0)} s^{(0)} T_0} (\frac{R_0}{r})^N$. Here, the superscript $^{(i=0,1,2,\ldots)}$ denotes the iteration number. Utilizing the initial fields $(P^{(0)}, T^{(0)}, v_n^{(0)})$, we can calculate all relevant He II thermodynamic variables and other needed parameters, such as $v_s^{(0)}$, $\rho^{(0)}$, $s^{(0)}$, $F_{ns}^{(0)}$, etc. These results allow us to iteratively update (P, T, v_n) as

$$P^{i+1} = P_b - \rho_s^i v_s^i(r)^2 - \rho_n^i v_n^i(r)^2 \tag{19}$$

$$T^{(i+1)}(r) = T_b + \int_{\infty}^{r} dr' G^{(i)}(r'), \tag{20}$$

$$v_n^{(i+1)}(r) = \frac{q_0}{\rho^{(0)} s^{(0)} T_0} \left(\frac{R_0}{r}\right)^N + \frac{I^{(i)}(r)}{r^N \rho^{(i)} s^{(i)}}. \tag{21}$$

The iteration is terminated once the relative change in the temperature field between consecutive iterations, defined as $|T^{(i)} - T^{(i-1)}|/T^{(i)}$, becomes less than 10^{-5} at all r. In the simulation, the integrals are performed using Simpson's rule with a step size of $\Delta r = 10$ μm [49].

As an example, we consider a cylindrical heater with a radius $R_0 = 0.2$ cm, subject to a constant surface heat flux q_0, as depicted in Fig. 1(a). We set $T_b = 1.78$ K and $h = 50$ cm and compute the steady-state profiles of $T(r)$, $L(r)$, and $v_n(r)$ using the iterative method outlined earlier. The results for q_0 close to 9.39 W/cm^2 are shown in Fig. 1(b). It is clear that approaching the heater, $T(r)$, $L(r)$, and $v_n(r)$ all increase rapidly towards their maximum values at $r = R_0$. In Fig. 1(c), we show the state parameters (T_0, P_0) of the He II on the heater surface at various q_0. The blue dot represents the state $(T_0 = T_b, P_0 = P_b)$ at $q_0 = 0$. As q_0 increases, the state approaches the saturation line of He II. The slight reduction in pressure is due to the Bernoulli effect incorporated in Eq. (11). At the peak heat flux $q^* \approx 9.39$ W/cm^2, the He II state on the heater surface reaches the saturation line. Beyond this point, vapor bubbles can be nucleated on the heater surface, which eventually leads to the formation of a vapor film covering the heater surface. The dynamics of the boiling process is beyond the scope of this paper. We shall treat q^* as the heat flux at which boiling occurs spontaneously.

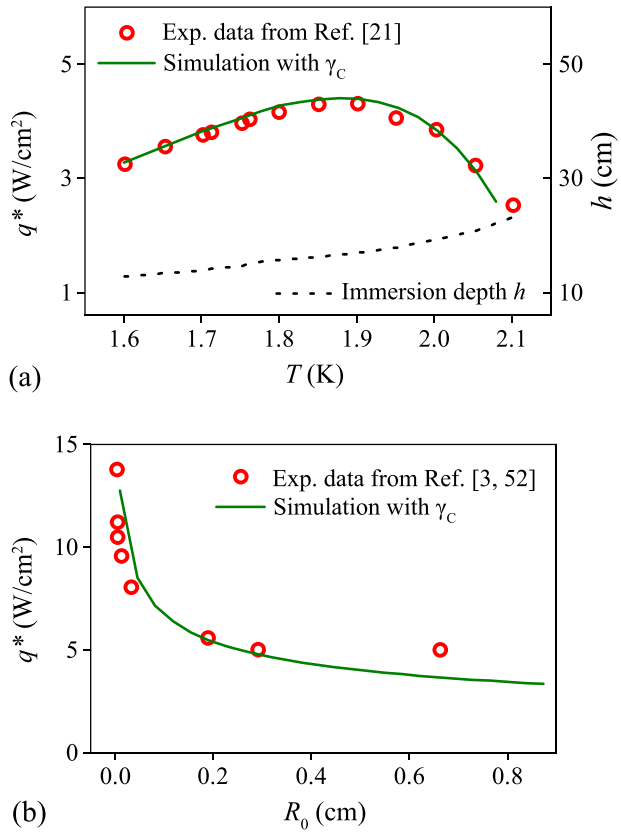

FIG. 2. (a) Comparison of simulated peak heat flux q^* at different He II bath temperature T_b with experimental data from Ref. [21] for a cylindrical heater with $R_0 = 0.66$ cm. The heater immersion depth h (dashed curve) varied with T_b in the experiment. (b) Simulated dependence of q^* on heater radius R_0 at $h = 10$ cm and $T_b = 1.78$ K, compared with experimental data from Refs. [3,52]. $\gamma_C = 1.2\gamma$ was adopted in these simulations.

III. MODEL CALIBRATION

To calibrate our model, we have looked into existing experimental research on q^* associated with steady-state nonuniform heat transfer in He II. There were several experimental studies on q^* for cylindrical heaters [17–21,50]. As for spherical heaters, research has been limited, primarily focusing on transient heat transfer scenarios or heat flux magnitudes considerably lower than q^* [22,51]. Among the available studies on q^* for cylindrical heaters, several studies employed thin-wire heaters with radii in the range of 1–10^2 μm [17–19], which is comparable to the mean vortex-line spacing $\ell = L^{-1/2}$ observed in such experiments. We choose to avoid those particular data sets in our study, since our coarse-grained model is applicable only at length scales much greater than ℓ. In subsequent analyses, we will focus on comparing our numerical simulation results with the data reported in Refs. [3,21,52], where cylindrical heaters of notable diameters were used.

Figure 2(a) presents the measured q^* values at different He II bath temperatures T_b for a cylindrical heater with $R_0 = 0.66$ cm [21]. In the referenced experiment, the immersion depth h declined as the bath was pumped to achieve lower T_b. Consequently, distinct T_b values correspond to varying h levels, as illustrated by the dotted curve in Fig. 2(a). Our model simulations have taken this variation into account. Figure 2(b) displays the measured q^* values for heaters with different radii R_0 at $T_b = 1.78$ K and $h = 10$ cm [3,52]. To compare with these data, we have calculated q^* under identical conditions using our iterative method. In our calculations, we adopted the γ coefficient derived from the He II heat conductivity function $f(T)$ under saturated vapor pressure, defined as [3]

$$f(T) = \frac{A_{GM}\rho_n}{\rho_s^3 s^4 T^3}, \tag{22}$$

where $A_{GM} \approx \frac{1}{3}\frac{\rho_n}{\rho}B_L\kappa\gamma^2$ is the Gorter–Melink mutual friction coefficient [5]. The expressions of f and A_{GM} lead to the following identity for γ:

$$\gamma = \sqrt{\frac{3\rho_s^3\rho s^4 T^3 f}{\rho_n \kappa B_L}}. \tag{23}$$

Experimentally, the temperature dependence of $f(T)$ in uniform counterflow has been studied thoroughly and its values are compiled in Ref. [3]. Therefore, the value of γ for uniform counterflow can be easily calculated. However, when it comes to nonuniform counterflow, there is little knowledge on how γ may change. In this context, we opt to scale the γ values deduced from Eq. (23) by a factor C, yielding $\gamma_C = C\gamma$. We treat C as an adjustable parameter. Remarkably, with $C = 1.2$, our simulation results (illustrated as solid curves in Fig. 2) exhibit excellent agreement with the experimental data. The optimized γ_C as a function of T is shown in Fig. 3 together with some γ values obtained in uniform counterflow experiments. In the subsequent sections, we will apply the optimized γ_C in our systematic analysis of q^*.

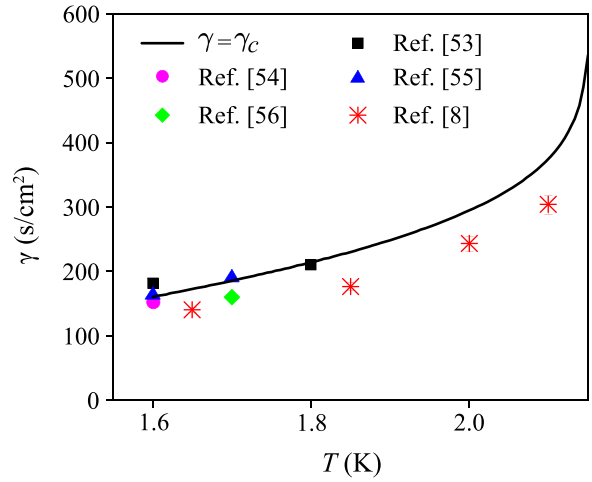

FIG. 3. Optimized γ_C as a function of T. Measured γ values in uniform counterflow in various experiments [8,53–56] are also shown.

IV. PEAK HEAT FLUX ANALYSIS

In this section, we present the simulated q^* values for steady-state counterflow produced by both cylindrical and spherical heaters, considering a variety of parameter combinations (T_b, h, R_0). We further demonstrate that q^* can be

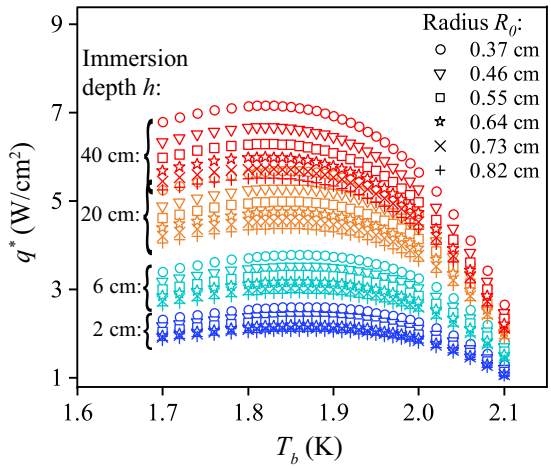

FIG. 4. Simulated peak heat flux q^* for cylindrical heaters with various T_b, h, and R_0.

calculated using an integral formula that involves the temperature difference between the heater surface and the bath. Using our simulation data, we can devise a correlation to evaluate this temperature difference, which in turn leads to a robust correlation for q^*.

A. Cylindrical heater case

Following the same procedures as illustrated in Fig. 1, we determined q^* as a function of T_b for cylindrical heaters of various R_0 and h values. These results are compiled in Fig. 4. It is evident that, at fixed R_0 and h values, q^* exhibits a nonmonotonic dependence on T_b, with a peak observed between 1.8 K and 1.9 K. On the other hand, at a fixed T_b, q^* consistently increases with an increase in h or a decrease in R_0.

To understand the behavior of q^*, we can refer to Eq. (12). For the parameter combinations (T_b, h, R_0) that we studied, we found that the terms on the left-hand side of Eq. (12) are typically more than two orders of magnitude smaller than the other terms across all values of r. If we dismiss these minor terms and utilize Eqs. (18) and (23), while noting that $v_{ns}(r) = q(r)/\rho_s sT$, the following equation can be derived:

$$\frac{dT}{dr} = -C^2 f(T) q^3(r). \tag{24}$$

In steady-state counterflow, $q(r)$ is given by $q(r) = q_0(R_0/r)^N$ (recall that $N = 1$ for cylindrical heaters and $N = 2$ for spherical heaters). When the heater surface heat flux q_0 reaches q^*, the above equation can be rearranged and integrated to produce an expression for q^*:

$$q^* = \left(\frac{3N-1}{C^2 R_0}\int_{T_b}^{T_b+\Delta T}\frac{dT}{f(T)}\right)^{1/3}, \tag{25}$$

where ΔT denotes the temperature increase on the heater surface relative to the He II bath at $q_0 = q^*$. This equation was introduced in Ref. [3]. However, due to the lack of information on how ΔT depends on (T_b, h, R_0), this equation was not employed to evaluate q^*.

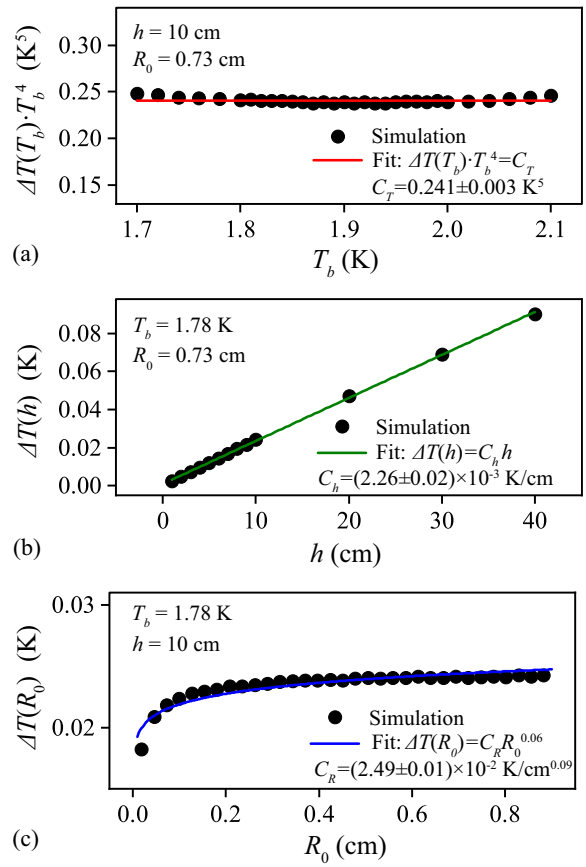

FIG. 5. (a) Simulated temperature rise ΔT on the heater surface as a function of T_b for a cylindrical heater with fixed h and R_0. (b) Dependence of ΔT on the immersion depth h at fixed T_b and R_0. (c) Dependence of ΔT on the heater radius R_0 at fixed T_b and h.

To facilitate the development of a practical correlation for q^*, we have computed ΔT values for all the cases depicted in Fig. 5. Some results showing the relationship of ΔT with T_b, h, R_0 are presented in panels (a), (b), and (c) of Fig. 5. From Fig. 5(a), we can see that, at fixed h and R_0, ΔT largely scales as T_b^{-4} across the entire bath temperature range we explored. Figure 5(b) demonstrates a rather good linear dependence of ΔT on h for given T_b and R_0. Lastly, Fig. 5(c) reveals a somewhat mild power-law dependence, $\Delta T \propto R_0^{\alpha}$, when T_b and h are fixed. This power exponent α varies with h and T_b, as listed in Table I, and is generally small. Combining all these insights, we can propose the following simple correlation between ΔT and the parameters T_b, h, and R_0:

$$\Delta T(T_b, h, R_0) = D\frac{hR_0^{\alpha}}{T_b^4}, \tag{26}$$

TABLE I. Fitted exponent α for cylindrical heaters.

h (cm)/T_b (K)	1.7	1.8	1.9	2.0
1	0.12	0.11	0.09	0.07
5	0.08	0.07	0.06	0.04
20	0.05	0.04	0.03	0.02

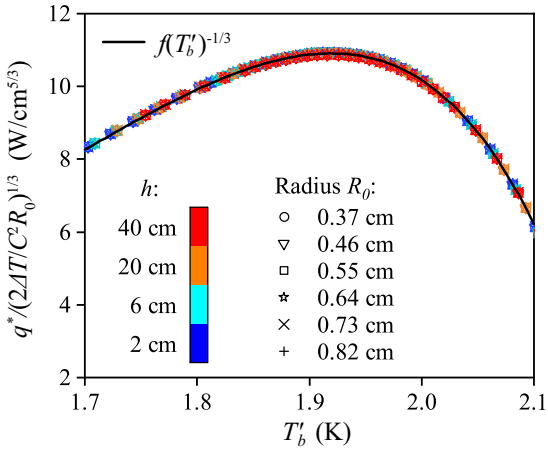

FIG. 6. Simulated $q^*/(2\Delta T/C^2R_0)^{1/3}$ as a function of $T_b' = T_b + \Delta T/2$ for cylindrical heaters at all the parameter combinations (T_b, h, R_0) we studied. The black curve represents $f^{-1/3}(T_b')$, where f is the known He II heat conductivity function [3]. The simulated data collapse nicely onto the $f^{-1/3}$ curve.

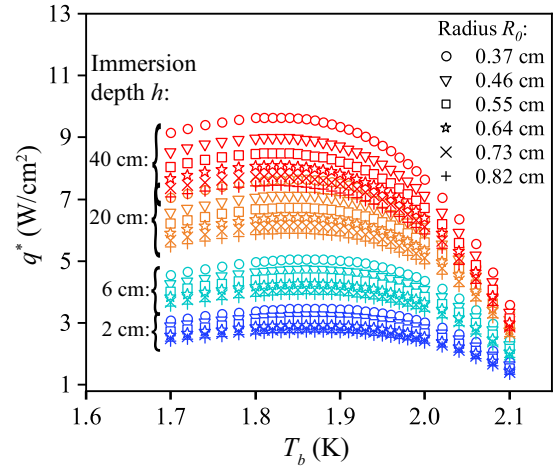

FIG. 7. Simulated peak heat flux q^* for spherical heaters with various T_b, h, and R_0.

where D is a numerical factor derivable from the scaling coefficients shown in Figs. 5(a)–5(c). To evaluate D in a more systematic manner, we compute it as $D = \Delta T/(hR_0^\alpha/T_b^4)$ for each parameter combination (T_b, h, R_0). Notably, within our chosen parameter range, all deduced values for D fall within the range $D = 0.024 \pm 0.002$ K^5/cm$^{1+\alpha}$. More details regarding the derivation of D is provided in the Appendix.

With the obtained expression for ΔT, we can now derive a convenient correlation to evaluate q^*. Given that ΔT is typically much smaller than T_b (i.e., see Fig. 5), the integral in Eq. (25) can be approximated by evaluating $f(T)$ at $T = T_b + \frac{1}{2}\Delta T$, resulting in

$$q^* \approx [(3N-1)\Delta T/C^2R_0]^{1/3} \cdot f(T_b + \Delta T/2)^{-1/3}. \quad (27)$$

To verify the accuracy of this expression for cylindrical heaters, we plot the simulated $q^*/(2\Delta T/C^2R_0)^{1/3}$ in Fig. 6 as a function of $T_b' = T_b + \Delta T/2$ for all the parameter combinations we studied. Impressively, all the simulated data collapse onto a single curve, which agrees precisely with $f(T_b')^{-1/3}$.

In order to derive a convenient correlation for q^* that explicitly depends on T_b, h, and R_0, one can perform a Taylor expansion of Eq. (27) as

$$q^* \approx (2\Delta T/C^2R_0)^{1/3}\left[\frac{1}{f(T_b)} - \frac{\Delta T}{2}\frac{f'(T_b)}{f(T_b)^2}\right]^{1/3}. \quad (28)$$

Using the expression for ΔT from Eq. (26), we can substitute it into Eq. (28) to yield the following final correlation:

$$q^* \approx \left[\frac{2Dh}{C^2R_0^{1-\alpha}T_b^4 f(T_b)}\left(1 - \frac{DhR_0^\alpha}{2T_b^4}\frac{f'(T_b)}{f(T_b)}\right)\right]^{\frac{1}{3}}. \quad (29)$$

With this correlation, evaluating q^* becomes straightforward given a specific set of parameters (T_b, h, R_0). It is worth noting from Eq. (29) that the dependence of q^* on R_0 can be expressed as $q^* \propto R_0^{-\frac{1}{m}}$, where $m \approx 3/(1-\alpha)$. For the parameter ranges explored in our simulations, m varies from 3.06 to 3.4. The deviation of m from 3 is entirely due to the weak dependence of ΔT on R_0, i.e., $\Delta T \propto R_0^\alpha$ as shown in Eq. (26). It is worth highlighting that such a deviation from $m = 3$ has indeed been reported experimentally [3].

B. Spherical heater case

In the case of spherical heaters, we follow a similar procedure to that for the cylindrical heaters. We consider a spherical heater of radius R_0 immersed at depth h in He II held at a bath temperature T_b and then conduct numerical simulations across various T_b, h, and R_0 values. The obtained q^* data are displayed in Fig. 7. From the data, it is evident that the variation of q^* with respect to T_b, h, and R_0 for spherical heaters shows similar trends observed for cylindrical heaters. Moreover, for a given parameter set (T_b, h, R_0), the q^* value for spherical heaters is consistently higher than that for cylindrical heaters.

The behavior of ΔT for spherical heaters closely mirrors what we observed for cylindrical heaters. In Figs. 8(a), 8(b), and 8(c), we display representative results showing the dependencies of ΔT on T_b, h, and R_0. These results lead us to a correlation for ΔT which strikingly takes the same form as Eq. (26) for cylindrical heaters, namely $\Delta T = D(hR_0^\alpha/T_b^4)$. The fitted values of α (as shown in Table II) are approximately double that of cylindrical heaters. The similarity of these expressions underscores the robustness of the correlation across different heater geometries. As before, the factor D for each parameter set (T_b, h, R_0) can be computed as $D = \Delta T/(hR_0^\alpha/T_b^4)$. The resulting values of D for all studied cases fall within $D = 0.024 \pm 0.002$ K^5/cm$^{1+\alpha}$, matching precisely with those derived for cylindrical heaters. Further details on the derivation of D are provided in the Appendix.

TABLE II. Fitted exponent α for spherical heaters.

h (cm)/T_b (K)	1.7	1.8	1.9	2.0
1	0.20	0.18	0.15	0.11
5	0.13	0.11	0.10	0.07
20	0.08	0.07	0.06	0.04

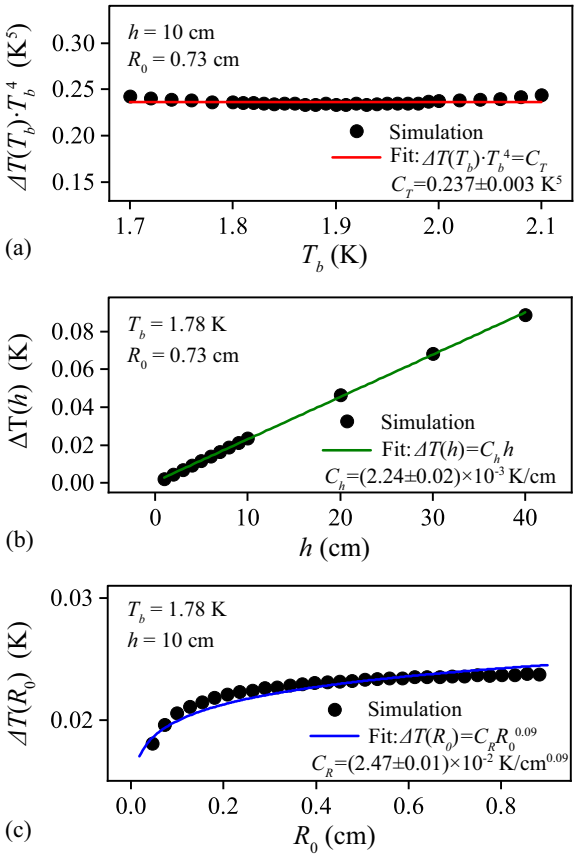

FIG. 8. (a) Dependence of ΔT on the bath temperature T_b for a spherical heater of fixed h and R_0. (b) Dependence of ΔT on the immersion depth h at fixed T_b and R_0. (c) Dependence of ΔT on the heater radius R_0 at fixed T_b and h.

To demonstrate the precision of Eq. (27) for spherical heaters, we again plot $q^*/(5\Delta T/C^2R_0)^{1/3}$ against $T_b' = T_b + \frac{1}{2}\Delta T$. As shown in Fig. 9, data points for all parameter combinations (T_b, h, R_0) collapse onto a single curve described by

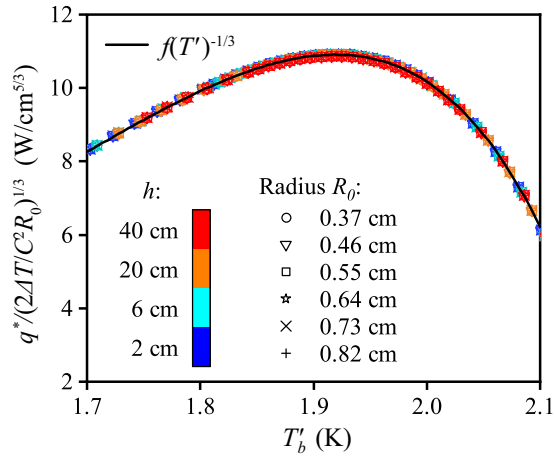

FIG. 9. Simulated $q^*/(2\Delta T/C^2R_0)^{1/3}$ as a function of $T_b' = T_b + \Delta T/2$ for spherical heaters at all the parameter combinations (T_b, h, R_0) we studied. The black curve represents $f^{-1/3}(T_b')$, where f is the known He II heat conductivity function [3].

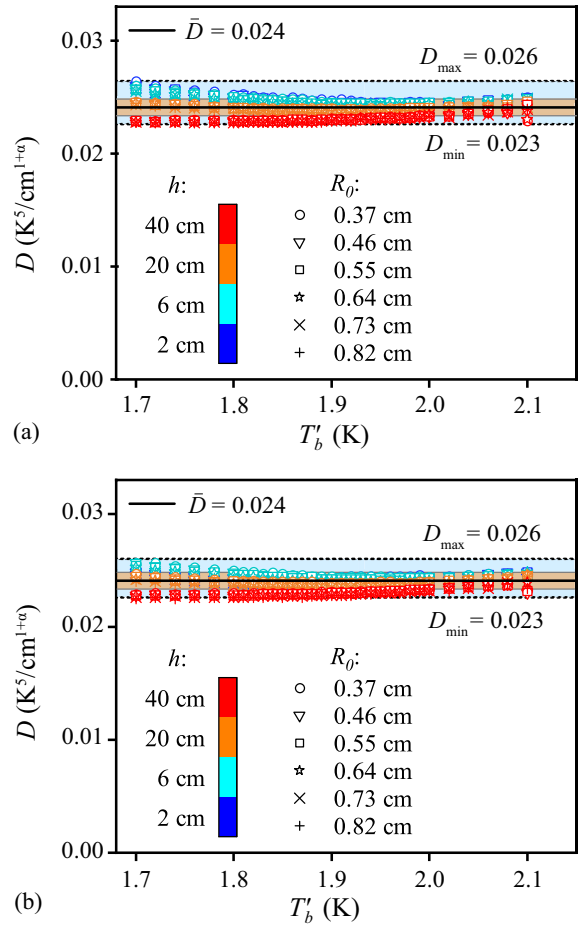

FIG. 10. Correlation factor D for (a) cylindrical and (b) spherical heaters, respectively, calculated under all the parameter combinations (T_b, h, R_0) we explored.

$f(T_b')^{-1/3}$. Finally, using a similar approach, we can express q^* for spherical heaters explicitly in terms of T_b, h, and R_0 by incorporating the expression for ΔT:

$$q^* \approx \left[\frac{5Dh}{C^2R_0^{1-\alpha}T_b^4 f(T_b)}\left(1 - \frac{DhR_0^\alpha}{2T_b^4}\frac{f'(T_b)}{f(T_b)}\right)\right]^{\frac{1}{5}}. \quad (30)$$

Compared to Eq. (29), apart from the variance in α, the main difference lies in the numerical factor $3N - 1 = 5$ for the spherical geometry.

V. SUMMARY

We have conducted a comprehensive numerical analysis of the boiling peak heat flux q^* for steady-state heat transfer in He II from both cylindrical and spherical heaters. The q^* value was calculated using the He II two-fluid equations of motion for given bath temperature T_b, heater immersion depth h, and heater radius R_0. We calibrated our model by comparing the simulated q^* values with available experimental data under the same parameter combinations (T_b, h, R_0). The optimized model was then utilized to generate q^* values across a wide parameter range. Based on the obtained data, we developed convenient correlations of q^* that explicitly depend on

(T_b, h, R_0) for both cylindrical and spherical heaters. Notably, while spherical heaters generally exhibit higher q^* values than their cylindrical counterparts under identical parameters, the derived correlations share a structural resemblance. These correlations are valuable in the design of cooling systems that involve steady but inhomogeneous heat transfer in He II. Looking ahead, we plan to extend the current work to evaluate q^* in transient heat transfer of He II in nonhomogeneous geometries. For such transient heat transfer, the correlation of q^* is expected to be more complicated, since it will depend not only on (T_b, h, R_0) but also the heating duration Δt. The insights obtained in the current research will form the foundation for our future transient heat transfer analysis.

ACKNOWLEDGMENTS

The authors acknowledge the support by the US Department of Energy under Grant No. DE-SC0020113 and the Gordon and Betty Moore Foundation through Grant No. GBMF11567. The work was conducted at the National High Magnetic Field Laboratory at Florida State University, which is supported by the National Science Foundation Cooperative Agreement No. DMR-2128556 and the state of Florida.

APPENDIX: DETERMINATION OF *D* FACTOR

In the main text, we discussed that the temperature rise $\Delta T = T_0 - T_b$ at the peak heat flux q^* can be expressed in terms of the bath temperature T_b, the hydrostatic head h, and the heater radius R_0 as given by Eq. (26). To determine D in a systematic manner, we calculate it as $D = \Delta T/(hR_0^\alpha/T_b^4)$ for each parameter combination (T_b, h, R_0). Figures 10(a) and 10(b) show the results for cylindrical and spherical heaters, respectively. The data cover a wide range of T_b, h, and R_0 and are indicated by distinct marker shapes and colors. It is clear that D remains roughly constant across all the parameter combinations. In each figure, two colored bands are shown. The narrow band shown in orange represents the region bounded by $D = \bar{D} \pm \sigma_D$, where $\bar{D} = 0.024$ K^5/cm$^{1+\alpha}$ is the mean value of D averaged over all the data points and σ_D denotes the standard deviation. The wide band shown in blue is bounded by the maximum $D_{\max} = 0.026$ K^5/cm$^{1+\alpha}$ and the minimum $D_{\min} = 0.023$ K^5/cm$^{1+\alpha}$ among all the data points. It is clear that all the D values fall within the range $D = 0.024 \pm 0.002$ K^5/cm$^{1+\alpha}$ across the parameter ranges considered in the paper, for both cylindrical and spherical heaters.

[1] D. R. Tilley and J. Tilley, *Superfluidity and Superconductivity*, 2nd ed., Graduate Student Series in Physics (Adam Hilger Ltd, Bristol, 1986).
[2] L. D. Landau and E. M. Lifshitz, *Fluid Mechanics*, 2nd ed. (Pergamon Press, Oxford, 1987), Vol. 6.
[3] S. W. Van Sciver, *Helium Cryogenics*, 2nd ed., International Cryogenics Monograph Series (Springer, New York, 2012).
[4] W. F. Vinen, Mutual friction in a heat current in liquid helium II I. experiments on steady heat currents, Proc. R. Soc. London A **240**, 114 (1957).
[5] R. J. Donnelly, *Quantized Vortices in Helium II* (Cambridge University Press, Cambridge, UK, 1991).
[6] W. F. Vinen, Mutual friction in a heat current in liquid helium II. II. experiments on transient effects, Proc. R. Soc. A **240**, 128 (1957).
[7] A. Marakov, J. Gao, W. Guo, S. W. Van Sciver, G. G. Ihas, D. N. McKinsey, and W. F. Vinen, Visualization of the normal-fluid turbulence in counterflowing superfluid ^{4}He, Phys. Rev. B **91**, 094503 (2015).
[8] J. Gao, E. Varga, W. Guo, and W. F. Vinen, Energy spectrum of thermal counterflow turbulence in superfluid helium-4, Phys. Rev. B **96**, 094511 (2017).
[9] J. Gao, W. Guo, S. Yui, M. Tsubota, and W. F. Vinen, Dissipation in quantum turbulence in superfluid ^{4}He above 1 K, Phys. Rev. B **97**, 184518 (2018).
[10] S. Bao, W. Guo, V. S. L'vov, and A. Pomyalov, Statistics of turbulence and intermittency enhancement in superfluid ^{4}He counterflow, Phys. Rev. B **98**, 174509 (2018).
[11] B. Mastracci and W. Guo, Exploration of thermal counterflow in He II using particle tracking velocimetry, Phys. Rev. Fluids **3**, 063304 (2018).
[12] W. Fiszdon and M. v. Schwerdtner, Influence of quantum turbulence on the evolution of moderate plane second sound heat pulses in helium II, J. Low Temp. Phys. **75**, 253 (1989).
[13] W. Fiszdon, M. von Schwerdtner, G. Stamm, and W. Poppe, Temperature overshoot due to quantum turbulence during the evolution of moderate heat pulses in He II, J. Fluid Mech. **212**, 663 (1990).
[14] T. Shimazaki, M. Murakami, and T. Iida, Second sound wave heat transfer, thermal boundary layer formation and boiling: Highly transient heat transport phenomena in He II, Cryogenics **35**, 645 (1995).
[15] D. K. Hilton and S. W. Van Sciver, Direct measurements of quantum turbulence induced by second sound shock pulses in helium II, J. Low Temp. Phys. **141**, 47 (2005).
[16] P. Zhang, M. Murakami, and R. Z. Wang, Study of the transient thermal wave heat transfer in a channel immersed in a bath of superfluid helium, Int. J. Heat Mass Transf. **49**, 1384 (2006).
[17] G. P. Lemieux and A. C. Leonard, Maximum and minimum heat flux in helium II for a 76.2 μ diameter horizontal wire at depths of immersion up to 70 centimeters, in *Advances in Cryogenic Engineering* (Springer US, Boston, MA, 1995), pp. 624–631.
[18] T. H. K. Frederking and R. L. Haben, Maximum low temperature dissipation rates of single horizontal cylinders in liquid helium II, Cryogenics **8**, 32 (1968).
[19] M. Shiotsu, K. Hata, and A. Sakurai, Effect of test heater diameter on critical heat flux in He II, in *Advances in Cryogenic Engineering*, edited by P. Kittel (Springer US, Boston, MA, 1994), pp. 1797–1804.
[20] J. S. Goodling and R. K. Irey, Non-boiling and film boiling heat transfer to a saturated bath of liquid helium, Adv. Cryog. Eng **14**, 159 (1969).
[21] S. W. Van Sciver and R. L. Lee, Heat transfer to helium-II in cylindrical geometries, Adv. Cryog. Eng. **35**, 363 (1980).
[22] A. P. Kryukov and A. F. Mednikov, Experimental study of He-II boiling on a sphere, J. Appl. Mech. Tech. Phys. **47**, 836 (2006).
[23] W. A. Maksoud, B. Baudouy, J. Belorgey, P. Bredy, P. Chesny, A. Donati, F. P. Juster, H. Lannou, C. Meuris, F. Molinie,

T. Schild, and L. Vieillard, Quench experiments in a 8-T superconducting coil cooled by superfluid helium, IEEE Trans. Appl. Supercond. **20**, 1989 (2010).

[24] M. D. G. Xavier, J. Schundelmeier, T. Winkler, T. Koettig, R. van Weelderen, and J. Bremer, Transient heat transfer in superfluid helium cooled Nb_3 Sn superconducting coil samples, IEEE Trans. Appl. Supercond. **29**, 1 (2019).

[25] S. Bao and W. Guo, Quench-spot detection for superconducting accelerator cavities via flow visualization in superfluid helium-4, Phys. Rev. Appl. **11**, 044003 (2019).

[26] S. Bao, T. Kanai, Y. Zhang, L. N. Cattafesta III, and W. Guo, Stereoscopic detection of hot spots in superfluid ^{4}He (He II) for accelerator-cavity diagnosis, Int. J. Heat Mass Transf. **161**, 120259 (2020).

[27] D. Durì, C. Baudet, J.-P. Moro, P.-E. Roche, and P. Diribarne, Hot-wire anemometry for superfluid turbulent coflows, Rev. Sci. Instrum. **86**, 025007 (2015).

[28] S. Bao and W. Guo, Transient heat transfer of superfluid ^{4}He in nonhomogeneous geometries: Second sound, rarefaction, and thermal layer, Phys. Rev. B **103**, 134510 (2021).

[29] H. Sanavandi, M. Hulse, S. Bao, Y. Tang, and W. Guo, Boiling and cavitation caused by transient heat transfer in superfluid helium-4, Phys. Rev. B **106**, 054501 (2022).

[30] S. K. Nemirovskii and W. Fiszdon, Chaotic quantized vortices and hydrodynamic processes in superfluid helium, Rev. Mod. Phys. **67**, 37 (1995).

[31] S. K. Nemirovskii, On the closure problem of the coarse-grained hydrodynamics of turbulent superfluids, J. Low Temp. Phys. **201**, 254 (2020).

[32] H. E. Hall and W. F. Vinen, The rotation of liquid helium II: I. experiments on the propagation of second sound in uniformly rotating helium II, Proc. R. Soc. London A **238**, 204 (1956).

[33] H. E. Hall and W. F. Vinen, The rotation of liquid helium II: II. the theory of mutual friction in uniformly rotating helium II, Proc. R. Soc. London A **238**, 215 (1956).

[34] R. J. Donnelly and C. F. Barenghi, The observed properties of liquid helium at the saturated vapor pressure, J. Phys. Chem. Ref. Data **27**, 1217 (1998).

[35] K. W. Schwarz, Three-dimensional vortex dynamics in superfluid ^{4}He: Homogeneous superfluid turbulence, Phys. Rev. B **38**, 2398 (1988).

[36] S. K. Nemirovskii, Macroscopic dynamics of superfluid turbulence, Low Temp. Phys. **45**, 841 (2019).

[37] I. M. Khalatnikov, *An Introduction to the Theory of Superfluidity*, 1st ed. (CRC Press, Boca Raton, FL, 2000).

[38] V. D. Arp, R. D. McCarty, and B. A. Hands, HEPAK - Thermophysical properties of helium from 0.8K or the melting line to 1500K, Cryodata Inc., 2005, https://htess.com/hepak/.

[39] S. Yui, H. Kobayashi, M. Tsubota, and W. Guo, Fully coupled two-fluid dynamics in superfluid ^{4}He: Anomalous anisotropic velocity fluctuations in counterflow, Phys. Rev. Lett. **124**, 155301 (2020).

[40] B. Mastracci, S. Bao, W. Guo, and W. F. Vinen, Particle tracking velocimetry applied to thermal counterflow in superfluid ^{4}He: Motion of the normal fluid at small heat fluxes, Phys. Rev. Fluids **4**, 083305 (2019).

[41] Y. Tang, W. Guo, H. Kobayashi, S. Yui, M. Tsubota, and T. Kanai, Imaging quantized vortex rings in superfluid helium to evaluate quantum dissipation, Nat. Commun. **14**, 2941 (2023).

[42] Y. A. Sergeev and C. F. Barenghi, Turbulent radial thermal counterflow in the framework of the HVBK model, Europhys. Lett. **128**, 26001 (2019).

[43] M. S. Mongiovì, D. Jou, and M. Sciacca, Non-equilibrium thermodynamics, heat transport and thermal waves in laminar and turbulent superfluid helium, Phys. Rep. **726**, 1 (2018).

[44] D. Khomenko, L. Kondaurova, V. S. L'vov, P. Mishra, A. Pomyalov, and I. Procaccia, Dynamics of the density of quantized vortex lines in superfluid turbulence, Phys. Rev. B **91**, 180504(R) (2015).

[45] S. K. Nemirovskii, Nonuniform quantum turbulence in superfluids, Phys. Rev. B **97**, 134511 (2018).

[46] R. K. Childers and J. T. Tough, Critical velocities as a test of the vinen theory, Phys. Rev. Lett. **31**, 911 (1973).

[47] J. T. Tough, *Superfluid turbulence*, Progress in Low Temperature Physics Vol. 8 (North-Holland, Amsterdam, 1982), Chap. 3.

[48] H. Adachi, S. Fujiyama, and M. Tsubota, Steady-state counterflow quantum turbulence: Simulation of vortex filaments using the full Biot-Savart law, Phys. Rev. B **81**, 104511 (2010).

[49] K. F. Riley, M. P. Hobson, and S. J. Bence, *Mathematical Methods for Physics and Engineering: A Comprehensive Guide*, 3rd ed. (Cambridge University Press, Cambridge, UK, 2006).

[50] R. K. Irey, Heat transport in liquid helium II, in *Heat Transfer at Low Temperatures*, edited by W. Frost (Springer US, Boston, MA, 1975), pp. 325–355.

[51] Z. Xie, Y. Huang, F. Novotný, Š. Midlik, D. Schmoranzer, and L. Skrbek, Spherical thermal counterflow of He II, J. Low Temp. Phys. **208**, 426 (2022).

[52] S. W. Van Sciver and R. L. Lee, Heat transfer from circular cylinders in He II, in *Cryogenic Processes and Equipment in Energy Systems* (ASME Publication, New York, 1981), pp. 147–154.

[53] C. E. Chase, Thermal conduction in liquid helium II. I. temperature dependence, Phys. Rev. **127**, 361 (1962).

[54] P. E. Dimotakis and J. E. Broadwell, Local temperature measurements in supercritical counterflow in liquid helium II, Phys. Fluids **16**, 1787 (1973).

[55] K. P. Martin and J. T. Tough, Evolution of superfluid turbulence in thermal counterflow, Phys. Rev. B **27**, 2788 (1983).

[56] S. Babuin, M. Stammeier, E. Varga, M. Rotter, and L. Skrbek, Quantum turbulence of bellows-driven ^{4}He superflow: Steady state, Phys. Rev. B **86**, 134515 (2012).